GEOPHYSICS, VOL. 81, NO. 4 (JULY-AUGUST 2016); P. S151–S163, 13 FIGS.
10.1190/GEO2015-0486.1

CrossMark
click for updates

Downloaded 07/18/16 to 138.67.12.184. Redistribution subject to SEG license or copyright; see Terms of Use at http://library.seg.org/

Acoustic wavefield imaging using the energy norm

Daniel Rocha[1], Nicolay Tanushev[2], and Paul Sava[1]

ABSTRACT

Wavefield energy can be measured by the so-called energy norm. We have extended the concept of "norm" to obtain the energy inner product between two related wavefields. Considering an imaging condition as an inner product between the source and receiver wavefields at each spatial location, we have developed a new imaging condition that represents the total reflection energy. Investigating this imaging condition further, we have found that it accounts for wavefield directionality in space time. Based on the directionality discrimination provided by this imaging condition, we have applied it to attenuate backscattering artifacts in reverse time migration (RTM). This imaging condition can be designed not only to attenuate backscattering artifacts, but also to attenuate any selected reflection angle. By exploiting the flexibility of this imaging condition for attenuating certain angles, we have developed a procedure to preserve the type of events that propagate along the same path, i.e., backscattered, diving, and head waves, leading to a suitable application for full-waveform-inversion (FWI). This application involves filtering the FWI gradient to preserve the tomographic term (waves propagating in the same path) and attenuate the migration term (reflections) of the gradient. We have developed the energy imaging condition applications for RTM and FWI using numerical experiments in simple (horizontal reflector) and complex models (Sigsbee and Marmousi).

INTRODUCTION

Wavefield extrapolation is commonly known as a mathematical technique for numerically generating a wavefield in space and time, using a known portion of the wavefield itself (Margrave and Ferguson, 1999). One can use wavefield extrapolation to form an image of the subsurface, which is related to the earth's reflectivity, in cases in which the velocity is known and sufficiently accurate or to obtain subsurface velocity information by solving an inverse problem. In particular, when the two-way wave equation is used, the former method is called reverse time migration (RTM) (Baysal et al., 1983; McMechan, 1983; Levin, 1984), and the latter is called full-waveform inversion (FWI) (Lailly, 1983; Tarantola, 1984; Gauthier et al., 1986; Plessix et al., 2013).

Reverse time migration (RTM), as well as other wave-equation imaging procedures, obtains an image of a reflector in the subsurface in two steps. The first step is to extrapolate two wavefields from surface seismic data: one originating at the source location and the other at receiver locations. The second step is to crosscorrelate these extrapolated wavefields in time and form an image as the zero-lag correlation (Clærbout, 1985). This procedure is based on the assumption that, for the single scattering approximation, the reflector is at the location where source and receiver wavefields coexist in time and space (Cohen and Bleistein, 1979; Oristaglio, 1989; Perrone and Sava, 2015). At the source location, the real injected pressure function is often unknown and an estimated source function is used; i.e., the source wavefield is synthetic for the majority of RTM implementations.

Full-waveform inversion (FWI) using two-way wave equation obtains a velocity update by crosscorrelation between the state wavefield, which is similar to the source wavefield in RTM, and the adjoint wavefield (Tarantola, 1984; Hindlet and Kolb, 1988; Plessix, 2006). The adjoint wavefield is extrapolated from a data residual, which is often defined as the difference between observed and synthetic data. The velocity model is updated by minimizing the residual in a least-squares sense. Mathematically, this velocity update is associated with the gradient of an objective function, which represents a norm of the residual vector.

The RTM and FWI methods rely on the crosscorrelation of wavefields, which causes some problems. On the one hand, besides imaging reflectors, RTM also outputs spurious artifacts caused by the crosscorrelation of wavefields propagating in the same direction: backscattering, head, and diving waves (Diaz and Sava, 2015). For FWI, on the other hand, the crosscorrelation of wavefields

Manuscript received by the Editor 14 September 2015; revised manuscript received 3 January 2016; published online 19 May 2016.
[1]Center for Wave Phenomena, Colorado School of Mines, Golden, Colorado, USA. E-mail: drocha@mines.edu; psava@mines.edu.
[2]Z-Terra Inc., Houston, Texas, USA. E-mail: nicktan@z-terra.com.
© 2016 Society of Exploration Geophysicists. All rights reserved.

Downloaded 07/18/16 to 138.67.12.184. Redistribution subject to SEG license or copyright; see Terms of Use at http://library.seg.org/

propagating in the same direction forms low-wavenumber events that translate into useful velocity update information (tomographic term), and the imaged reflectors (migration term) represent the source of nonlinearity that prevents the optimization from converging (Mora, 1989). Given these problems, alternatives to crosscorrelation have been investigated for RTM and FWI (Chang and McMechan, 1986; Fletcher et al., 2005; Gao et al., 2012).

For RTM, the simplest and most common approach for overcoming the low-wavenumber events is to apply a high-pass filter. The Laplacian filter serves this purpose (Youn and Zhou, 2001) and is also convenient regarding processing cost because it involves postimaging filtering. Other postimaging filtering techniques are shown in the literature (Guitton et al., 2007; Xu et al., 2014), but such techniques do not account for multipathing. This filtering can also be applied prior to imaging by using the propagation directions of wavefields obtained by Poynting vectors (Yoon and Marfurt, 2006; Costa et al., 2009), by optical flow (Vyas et al., 2011; Zhang, 2014), or by wavefield decomposition (Suh and Cai, 2009; Liu et al., 2011) to attenuate wavefields traveling in the same direction. However, the imaging condition using Poynting vectors requires the design of a weighting function, and wavefield decomposition only separates wavefields into their up- and downgoing parts, resulting in unaltered backscattering artifacts from nearly horizontal reflected waves.

For FWI, to preserve the tomographic component and attenuate the migration component in the velocity update, some authors use filtering on the FWI gradient (Almomin and Biondi, 2012; Albertin et al., 2013; Tang et al., 2013; Alkhalifah, 2015). All of these approaches use an extension of the gradient, similar to extended images in wave-equation migration (Sava and Fomel, 2006; Sava and Vasconcelos, 2011), to separate tomographic and migration components by exploiting the angle between the wave vectors and to mute the reflections from the gradient. With extended images, it is also possible to implement image-domain wavefield tomography using an objective function that penalizes energy away from zero lag (i.e., reflections) and preserves the backscattering energy, which is mostly present at zero lag (Diaz and Sava, 2015).

Considering these recurrent problems of crosscorrelation in RTM and FWI, we are motivated to find an imaging condition that is implemented by a simple operation between vectors that represent wavefield directionality. These vectors are defined in the 4D space time and can be made orthogonal for undesired events. Then, a simple dot product eliminates these events and preserves the reflectors (i.e., the image). This operation is simple to apply because it does not involve identifying specific propagation directions, as in the case for Poynting vector methods (Yoon and Marfurt, 2006).

The proposed imaging condition is also discussed by Tarantola (1984) in the context of waveform inversion using impedance as the model parameter. This imaging condition attenuates the backscattering and is related to the Laplacian filter, as shown by other authors (Douma et al., 2010; Whitmore and Crawley, 2012; Brandsberg-Dahl et al., 2013; Pestana et al., 2013; Sun and Wang, 2013). Although more general in nature, the imaging condition is ideally suited for backscattering filtering, as discussed later in this paper.

We start by reviewing the theory of energy conservation in 4D space time to develop the physical explanation of the proposed imaging condition. Then, we show how this imaging condition can be applied to RTM for attenuating the backscattering artifacts and to FWI for obtaining the tomographic term, free of reflection artifacts.

REVERSE TIME MIGRATION

In this section, we develop the theoretical aspects of the proposed imaging condition. We describe the conventional imaging condition (CIC) as an inner product between the source and receiver wavefields at each spatial location. Then, we formulate an alternative imaging condition based on the mechanical energy of the extrapolated wavefields. Appropriately modifying the inner product enables us to use it as an imaging condition to attenuate certain reflection angles and consequently, to attenuate backscattering artifacts from RTM images. Conversely, for transmission FWI, we attenuate the contribution of waves propagating at arbitrary angles and preserve the waves that propagate along the same paths.

The L_2-norm and the CIC

For a given seismic experiment with index e, consider a wavefield $U(e,\mathbf{x},t)$ as a solution to the acoustic wave equation

$$\ddot{U} - v^2\nabla^2 U = f, \tag{1}$$

where $v(\mathbf{x})$ is the medium velocity, the superscript dot indicates time differentiation, ∇^2 is the spatial Laplacian operator, and $f(e,\mathbf{x},t)$ is the source function. The experiment index e commonly refers to a shot record experiment for a certain source location $\mathbf{x}_s$.

If we, for example, try to evaluate how close to one another two wavefields are, a global measure of wavefield strength is of interest in wavefield imaging. Considering U is real valued, we can characterize the strength of the wavefield by the L_2-norm

$$\|U\|^2 = \sum_{e,\mathbf{x},t} U^2. \tag{2}$$

An application of this norm in wavefield imaging is present in data-domain wavefield tomography, where it is used to minimize the wavefield difference at the recorded data locations. Another application is in image-domain wavefield tomography, where the norm is used to minimize the energy away from zero lag in extended images (Yang and Sava, 2015). In linear algebra, a norm is also defined as the inner product of a vector with itself (Jain et al., 2004). Hence, one can define an L_2 inner product between the two wavefields $U(e,\mathbf{x},t)$ and $V(e,\mathbf{x},t)$ as

$$\langle U, V\rangle = \sum_{e,\mathbf{x},t} UV. \tag{3}$$

A common application of this L_2 inner product in wavefield imaging is to compare source and receiver wavefields $U(\mathbf{x},t)$ and $V(\mathbf{x},t)$, respectively, and to form an image $I(\mathbf{x})$ of the subsurface:

$$I = \sum_{e,t} UV. \tag{4}$$

Note that equation 4 is commonly known as the CIC, forming an image at every location where the wavefields coexist in space and time. However, the propagation directions of the different wavefields are not taken into account when forming the image. Consequently, the resulting image contains backscattering artifacts, which occur wherever source and receiver wavefields propagate along the same path. We illustrate this idea with the simple 2D theoretical

Downloaded 07/18/16 to 138.67.12.184. Redistribution subject to SEG license or copyright; see Terms of Use at http://library.seg.org/

experiment depicted in Figure 1. The rays from source and receiver wavefields are represented in the space-time continuum. When they backscatter at the reflector depth ($z = 2.5$ km) (Figure 1a and 1b), the CIC (dashed lines in Figure 1c) forms an image at all locations above the reflector where the wavefields coexist.

This imaging failure stems from the fact that the imaging condition does not account for the wavefield propagation direction. As indicated earlier, alternative imaging conditions attempt to address this challenge. In the following section, we use energy conservation laws and alternative wavefield norms to account for the wavefield propagation direction and we derive a new imaging condition that exploits not only the wavefield position and timing, but also its orientation.

The energy norm and the proposed imaging condition

One can define a measure of energy for a solution to the acoustic homogeneous wave equation within a spatial domain Ω (Evans, 1997; McOwen, 2003):

$$E(t) = \frac{1}{2}\int_{\Omega}[\dot{U}^2 + v^2|\nabla U|^2]d\mathbf{x}. \tag{5}$$

The time derivative term corresponds to the kinetic energy of the wavefield, and the spatial gradient term corresponds to its potential energy. The wavefield energy is conserved over time as seen by taking the derivative of equation 5 with respect to time:

$$\frac{1}{2}\frac{d}{dt}\int_{\Omega}[\dot{U}^2 + v^2|\nabla U|^2]d\mathbf{x} = \int_{\Omega}[\dot{U}\,\ddot{U} + v^2\nabla U\cdot\nabla\dot{U}]d\mathbf{x}. \tag{6}$$

Then, we apply the chain rule in the second term on the right side of equation 6 as

$$\int_{\Omega}[\nabla U\cdot\nabla\dot{U}]d\mathbf{x} = \int_{\Omega}\nabla\cdot(\dot{U}\nabla U)d\mathbf{x} - \int_{\Omega}(\dot{U}\nabla^2 U)d\mathbf{x}. \tag{7}$$

The first integral on the right side can be turned into a surface integral by the divergence theorem. Assuming homogeneous boundary conditions, i.e., the wavefield and its derivatives vanish on the boundary, we have

$$\int_{\Omega}\nabla\cdot(\dot{U}\nabla U)d\mathbf{x} = \int_{\delta\Omega}\dot{U}\,\nabla U d\mathbf{x} = 0. \tag{8}$$

Substituting the remaining term from equation 7 into equation 6 yields

$$\dot{E}(t) = \frac{1}{2}\int_{\Omega}\dot{U}(\ddot{U} - v^2\nabla^2 U)d\mathbf{x} = 0, \tag{9}$$

for a wavefield that satisfies the homogeneous wave equation in equation 1, thus indicating that the total energy of the wavefield is conserved.

A norm and an inner product in a vector space can be defined if they result in a scalar quantity and have linear properties. The energy norm is defined in this context as (Zeidler, 1999; Tanushev et al., 2009)

$$\|U\|_E^2 = \sum_{e,\mathbf{x},t}[\dot{U}^2 + v^2|\nabla U|^2], \tag{10}$$

and the respective inner product for two wavefields $U(e,\mathbf{x},t)$ and $V(e,\mathbf{x},t)$ is

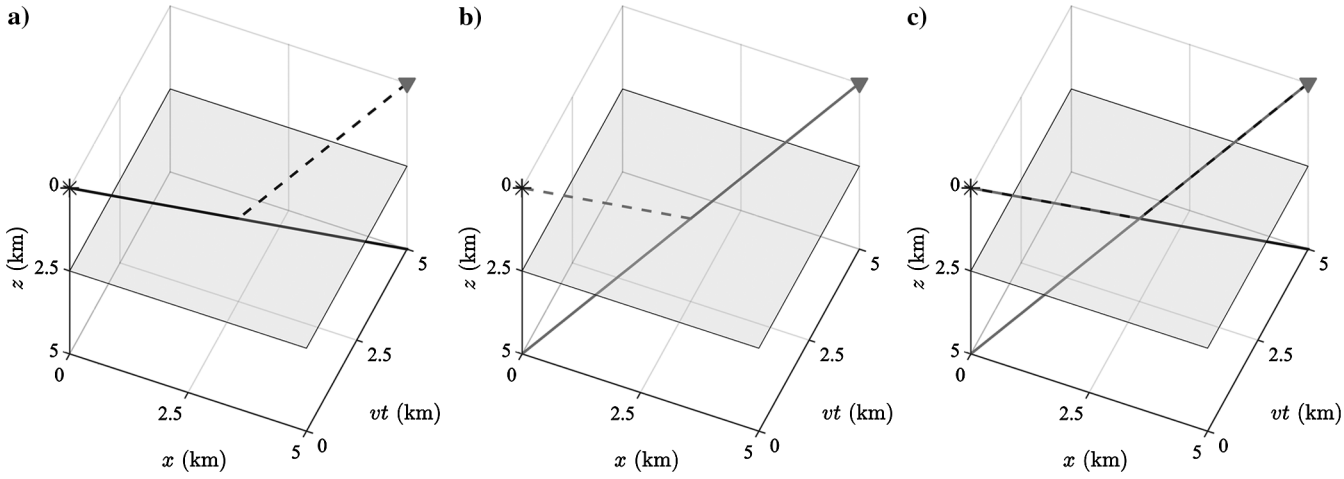


Figure 1. Schematic representation of (a) the source wavefield, (b) the receiver wavefield, and (c) conventional imaging in a 2D experiment for a horizontal reflector at $z = 2.5$ km, source at the origin (star symbol) and receiver at the surface and $x = 5$ km (triangle symbol). The backscattered waves from source and receiver wavefields coexist in space and time and, consequently, overlap in the conventional image.

$$\langle U, V\rangle_E = \sum_{e,\mathbf{x},t}(\dot{U}\,\dot{V} + v\nabla U \cdot v\nabla V). \tag{11}$$

Note that the inner product in equation 11 is composed of the dot product between the gradient vectors of the wavefields scaled by the velocity (v), plus the product of their time derivatives. The time dimension provides an additional derivative component beyond the components of the spatial gradient. Thus, a wavefield $U(\mathbf{x}, t)$ can be represented in a Euclidean space with spatial coordinates $\mathbf{x} = \{x, y, z\}$ and an additional coordinate vt. The gradient of U in this 4D space can be defined as follows:

$$\left(v\frac{\partial U}{\partial x}, v\frac{\partial U}{\partial y}, v\frac{\partial U}{\partial z}, \dot{U}\right). \tag{12}$$

Notice that the first three components of this vector form the conventional spatial gradient of the wavefield. The fourth component contains a time derivative, which is related to the temporal forward or backward character of the wavefield. Therefore, this vector indicates the space and time directionality of the wavefield at a particular position and time. This notion of a 4D gradient is used in other research areas, such as special relativity and wave theory, with the following compact notation (Feynman et al., 1964; Chappel et al., 2010):

$$\square U = (v\nabla U, \dot{U}). \tag{13}$$

We can rewrite equations 10 and 11 using the dot product between such 4D vectors:

$$\|U\|_E^2 = \|\square U\|^2 \tag{14}$$

$$\langle U, V\rangle_E = \langle \square U, \square V\rangle. \tag{15}$$

If the inner product in equation 11 is evaluated at each spatial location and the time-reversal aspect of the receiver wavefield is considered, which means this wavefield is oriented backward in time ($V(e, \mathbf{x}, T - t)$), we can define an imaging condition as

$$\begin{aligned} I_E &= \sum_{e,t} \square U \cdot \square V \quad \text{and} \\ &= \sum_{e,t}(\dot{U}\,\dot{V} + v\nabla U \cdot v\nabla V). \end{aligned} \tag{16}$$

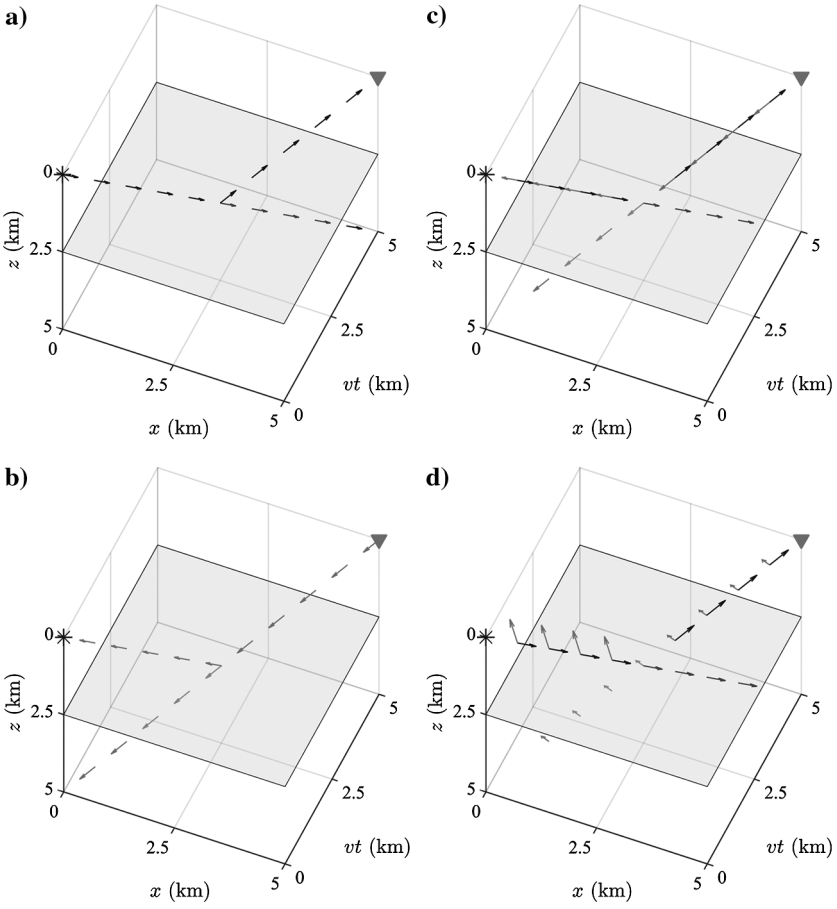


Figure 2. Schematic representation of the vector fields (a) $\square U$ originated from the source (star symbol), (b) $\square V$ originated from the receiver (triangle symbol), (c) the vector fields plotted together, and (d) the imaging condition in equation 26. Notice that in panel (d), the backscattering events are characterized by orthogonal vectors $\square U$ and $\square V$, whereas the reflections are characterized by nonorthogonal vectors $\square U$ and $\square V$.

The energy imaging condition forms an image at every location where the dot product between the vectors $\square U$ and $\square V$ is nonzero. Notice that the time derivatives should be evaluated in reverse time, considering that V is generated by an adjoint wave-equation operator. Figure 2 shows $\square U$ and $\square V$ for the theoretical experiment depicted in Figure 1. These figures show that these vectors describe the wavefield propagation direction in this space-time continuum. Notice that these vectors are not orthogonal for the backscattering events using the imaging condition in equation 16, and we need to slightly change the imaging condition for the purpose of preserving only the reflection information. To remove certain undesired events, such as backscattering artifacts, one can properly use this imaging condition to make their respective vectors $\square U$ and $\square V$ orthogonal to each other. In fact, this idea can be implemented to attenuate any event with a certain bisection angle.

Wavefield orientation in the imaging condition

Source and receiver wavefields can be decomposed in plane waves, which leads us to the reflection angle definition: the angle between the wavenumber vector of the plane wave and the normal to the reflector. For a given experiment, the Fourier transform of the wavefield is a function of the wavenumber vector and frequency

Downloaded 07/18/16 to 138.67.12.184. Redistribution subject to SEG license or copyright; see Terms of Use at http://library.seg.org/

Downloaded 07/18/16 to 138.67.12.184. Redistribution subject to SEG license or copyright; see Terms of Use at http://library.seg.org/

$\tilde{U}(e,\mathbf{k},\omega)$. Using U and V transformed to the Fourier domain, one can apply the CIC as

$$I(\mathbf{k}) = \sum_{e,\omega} \tilde{U}\,\tilde{V}^*, \tag{17}$$

where $*$ is the complex conjugate operator in frequency. The energy imaging condition uses the vectors $\Box U$ and $\Box V$ in the time domain. In the Fourier domain, these vectors can be defined in the same way as shown in equation 13, but using the derivative operators with respect to frequency and wavenumber components:

$$\begin{aligned}\tilde{\Box U} &= (ivk_x\tilde{U}, ivk_y\tilde{U}, ivk_z\tilde{U}, -i\omega\tilde{U})\\ &= i(v\mathbf{k}_s, -\omega)\tilde{U}\end{aligned} \tag{18}$$

$$\begin{aligned}\tilde{\Box V} &= (ivk_x\tilde{V}^*, ivk_y\tilde{V}^*, ivk_z\tilde{V}^*, +i\omega\tilde{V}^*)\\ &= i(v\mathbf{k}_r, +\omega)\tilde{V}^*,\end{aligned} \tag{19}$$

considering that the adjoint derivative for V is the opposite to the forward derivative in the Fourier domain. Therefore, the dot product between $\tilde{\Box U}$ and $\tilde{\Box V}$ is

$$\begin{aligned}\tilde{\Box U}\cdot\tilde{\Box V} &= [-v^2(\mathbf{k}_s\cdot\mathbf{k}_r)+\omega^2]\tilde{U}\tilde{V}^*\\ &= [-v^2||\mathbf{k}_s||||\mathbf{k}_r||\cos 2\theta+\omega^2]\tilde{U}\tilde{V}^*,\end{aligned} \tag{20}$$

where 2θ is the reflection aperture angle and also the angle between the spatial gradient vectors. Using the dispersion relation

$$||\mathbf{k}_s|| = ||\mathbf{k}_r|| = \frac{\omega}{v} \tag{21}$$

in equation 20 leads to

$$\tilde{\Box U}\cdot\tilde{\Box V} = [-\omega^2\cos 2\theta+\omega^2]\tilde{U}\tilde{V}^*. \tag{22}$$

In equation 22, to attenuate a certain reflection of angle θ_c, we need to apply a scaling factor to the second term (product of the time derivatives of the wavefields), thus nullifying the term in the brackets:

$$\begin{aligned}\tilde{\Box U}\cdot\tilde{\Box V} &= [-\omega^2\cos 2\theta+\omega^2\cos 2\theta_c]\tilde{U}\tilde{V}^*\\ &= 0, \quad \text{if } \theta=\theta_c.\end{aligned} \tag{23}$$

Therefore, in the Fourier domain, the imaging condition with this angle factor is

$$\begin{aligned}I_E(\mathbf{k}) &= \sum_{e,\omega}\tilde{\Box U}\cdot\tilde{\Box V} \quad \text{and}\\ &= \sum_{e,\omega}[\omega^2\cos 2\theta_c - v^2(\mathbf{k}_s\cdot\mathbf{k}_r)]\tilde{U}\tilde{V}^*.\end{aligned} \tag{24}$$

In the space-time domain, we can modify the imaging condition in equation 16 by including the angle factor:

$$I_E = \sum_{e,t}(\cos(2\theta_c)\dot{U}\,\dot{V} + v\nabla U\cdot v\nabla V). \tag{25}$$

Backscattering attenuation

The backscattering artifact, in particular, is not a reflection. However, its wavenumber vectors $\mathbf{k_s}$ and $\mathbf{k_r}$ are collinear and opposite, with an angle of 180° between them. The artifact can be treated as having a 90° reflection angle, which implies that $\cos 2\theta_c = -1$. Therefore, we can rewrite equation 25 to form an imaging condition specifically designed to attenuate the backscattering energy:

$$I_E = \sum_{e,t}(-\dot{U}\,\dot{V} + v\nabla U\cdot v\nabla V). \tag{26}$$

Figure 2d shows the vectors $\Box U$ and $\Box V$ for the imaging condition in equation 26. Notice that, for the backscattering artifacts, these vectors are orthogonal, which makes their dot product zero. This means that the backscattered energy is attenuated and reflectors are preserved if we apply the imaging condition in equation 26.

The attenuation of the backscattering artifacts is one practical benefit of the energy imaging condition over its conventional L_2 counterpart. The Laplacian operator applied on the conventional image is the most common form of backscattering filtering. The proposed imaging condition is related to the Laplacian filter by (Appendix A)

$$I_E = \frac{1}{2}\nabla^2 I_{L_2}. \tag{27}$$

Therefore, the proposed imaging condition is the general form of the filtering using the Laplacian operator for any reflection angle θ_c.

Amplitude and phase of the energy imaging condition

Compared to the CIC, the angle between $\Box U$ and $\Box V$ influences the amplitude of the energy image, whereas in CIC the amplitude of the image only depends on the strength of U and V. Using I_E from equation 24 for the special case when $\cos 2\theta_c = -1$, we have

$$I_E = -\sum_{e,\omega}\omega^2[1+\cos 2\theta]\tilde{U}\tilde{V}^*. \tag{28}$$

Following the strategy from Zhang and Sun (2009), to preserve the phase compared to the CIC image, one can integrate the source function and receiver data before wavefield extrapolation, which means scaling I_E by $1/\omega^2$ in the frequency domain. The amplitude of the resulting image is not exactly equal to the amplitude in CIC due to the term depending on the reflection angle $1+\cos 2\theta$. Only if the reflection angle is known for each time and space location of the correlated wavefields can one multiply I_E by $-1/(\omega^2[1+\cos 2\theta])$ to get the exact amplitude and phase of CIC. This is also true for the Laplacian filter, and we can obtain the expression from Zhang and Sun (2009) starting from equation 27:

$$-\sum_{\omega}2\omega^2[1+\cos 2\theta]\tilde{U}\tilde{V}^* = -v^2||\mathbf{k}||^2\sum_{\omega}\tilde{U}\,\tilde{V}^*. \tag{29}$$

Using the trigonometric identity

$$1+\cos 2\theta = 2\cos^2\theta, \tag{30}$$

Downloaded 07/18/16 to 138.67.12.184. Redistribution subject to SEG license or copyright; see Terms of Use at http://library.seg.org/

we obtain from equation 29 the following relation:

$$\|\mathbf{k}\|^2 = \frac{4\omega^2 \cos^2\theta}{v^2}, \tag{31}$$

which means that the Laplacian filter also has a term that depends on the reflection angle θ.

Another particular case is when the energy imaging condition is used to attenuate normal-incidence reflections ($\cos 2\theta_c = 1$). Using equation 24 and the following trigonometric identity

$$1 - \cos 2\theta = 2\sin^2\theta, \tag{32}$$

we obtain the following pair of imaging conditions:

$$I_E(\mathbf{k}, \theta_c = 0^\circ) = +2\sum_{e,\omega} \omega^2 \sin^2(\theta)\tilde{U}\tilde{V}^* \tag{33}$$

$$I_E(\mathbf{k}, \theta_c = 90^\circ) = -2\sum_{e,\omega} \omega^2 \cos^2(\theta)\tilde{U}\tilde{V}^*, \tag{34}$$

whose difference multiplied by $1/\omega^2$ is equivalent to the conventional image. The imaging conditions in equations 33 and 34 are conveniently implemented in the time domain:

$$I_E(\mathbf{x}, \theta_c = 0^\circ) = \sum_{e,t} (\dot{U}\,\dot{V} + v\nabla U \cdot v\nabla V) \tag{35}$$

$$I_E(\mathbf{x}, \theta_c = 90^\circ) = \sum_{e,t} (-\dot{U}\,\dot{V} + v\nabla U \cdot v\nabla V), \tag{36}$$

Later in this paper, we exploit the complementary behavior of these two imaging conditions.

Examples

With simple synthetic examples, we illustrate the application of the proposed imaging condition. Then, we show its effectiveness with a complex model (Sigsbee).

Figure 3 shows a simple experiment with a flat reflector at $z = 2$ km, a velocity with a low-velocity Gaussian anomaly (Figure 3a), with one source and one receiver on the surface at $x = 2.5$ km and $x = 7.5$ km, respectively. The Gaussian anomaly is added in the

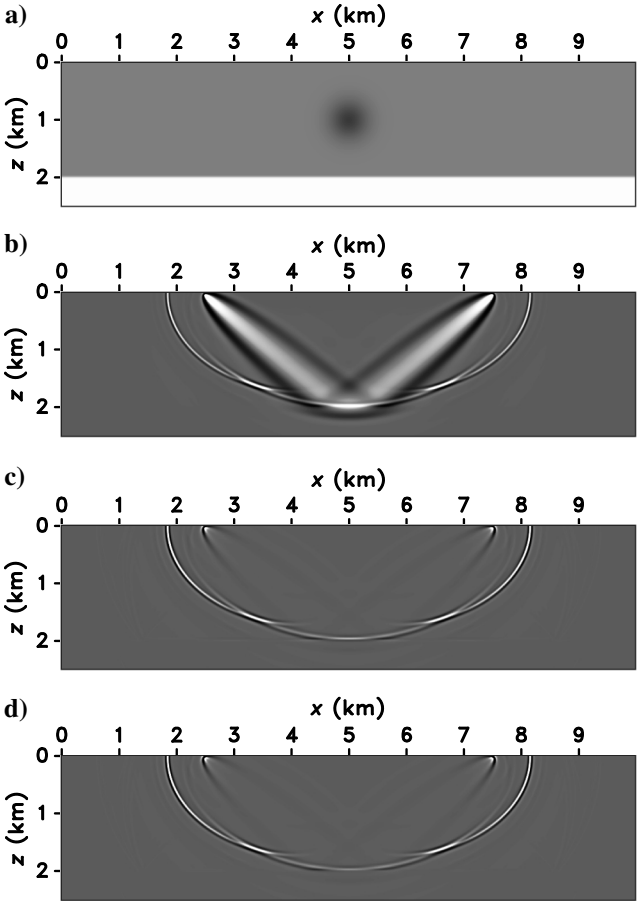


Figure 3. Experiment with a flat reflector, one source and one receiver on the surface at the locations $x = 2.5$ km and $x = 7.5$ km, respectively: (a) velocity model, with a low-velocity Gaussian anomaly; (b) CIC, and (c) with Laplacian filter applied; (d) energy imaging condition.

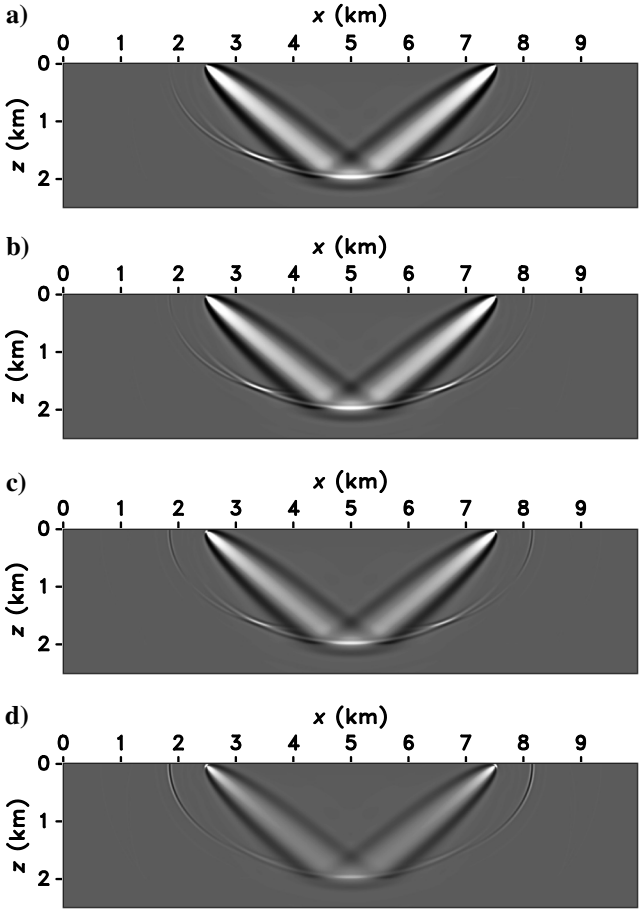


Figure 4. Same experiment geometry and model from Figure 3, but using the energy norm imaging condition to attenuate certain reflection angles: (a) normal-incidence reflections, (b) 15° reflections, (c) 30° reflections, and (d) 45° reflections.

Downloaded 07/18/16 to 138.67.12.184. Redistribution subject to SEG license or copyright; see Terms of Use at http://library.seg.org/

velocity to generate wavefield triplications and therefore, test the efficiency of the imaging condition when multipathing occurs. As expected, the conventional image (Figure 3b) shows backscattering artifacts, which are very strong along the path at the 45° reflection angle. The Laplacian filter applied on the conventional image (Figure 3c) attenuates backscattering artifacts. The energy image in Figure 3d, which uses the imaging condition in equation 26, shows a similar result compared to Figure 3c, proving the equivalency of these images for the far-field.

Figure 4 shows the application of the imaging condition in equation 25. In these images, every reflection of a certain angle is attenuated by scaling the time-derivative product by $\cos(2\theta_c)$. This proves that our new imaging condition can be used to attenuate reflections for arbitrary angles. Later in this paper, we describe a specific application exploiting this generalization.

Figure 5 shows imaging results from selected single shots using these different imaging conditions for the Sigsbee model. Stacking all individual migrated images, we obtain the migrated images in Figure 6. Figure 6a shows the stratigraphic velocity model that was used to generate the synthetic data for the experiment. The conventional image in Figure 6b is masked by the low-frequency backscattered energy. The application of the energy norm imaging condition removes the low-frequency artifacts in Figure 6c.

FULL-WAVEFORM INVERSION

The same methodology applied in the preceding section for migration can also be applied to waveform inversion. The gradient of the objective function (required to update the velocity) is equivalent to an RTM image of the data difference, instead of the data themselves, if the adjoint-state method is implemented (Plessix et al., 1998). We begin this section by reviewing the adjoint-state method. Then, we use the energy norm to obtain the inner product between state and adjoint variables, which is required in the calculation of the objective function gradient. Modifying the inner product properly, we are able to filter the gradient and preserve the tomographic term while attenuating the migration term.

Adjoint-state method

Data-domain wavefield tomography consists of comparing simulated and observed wavefields at specific data locations, improving

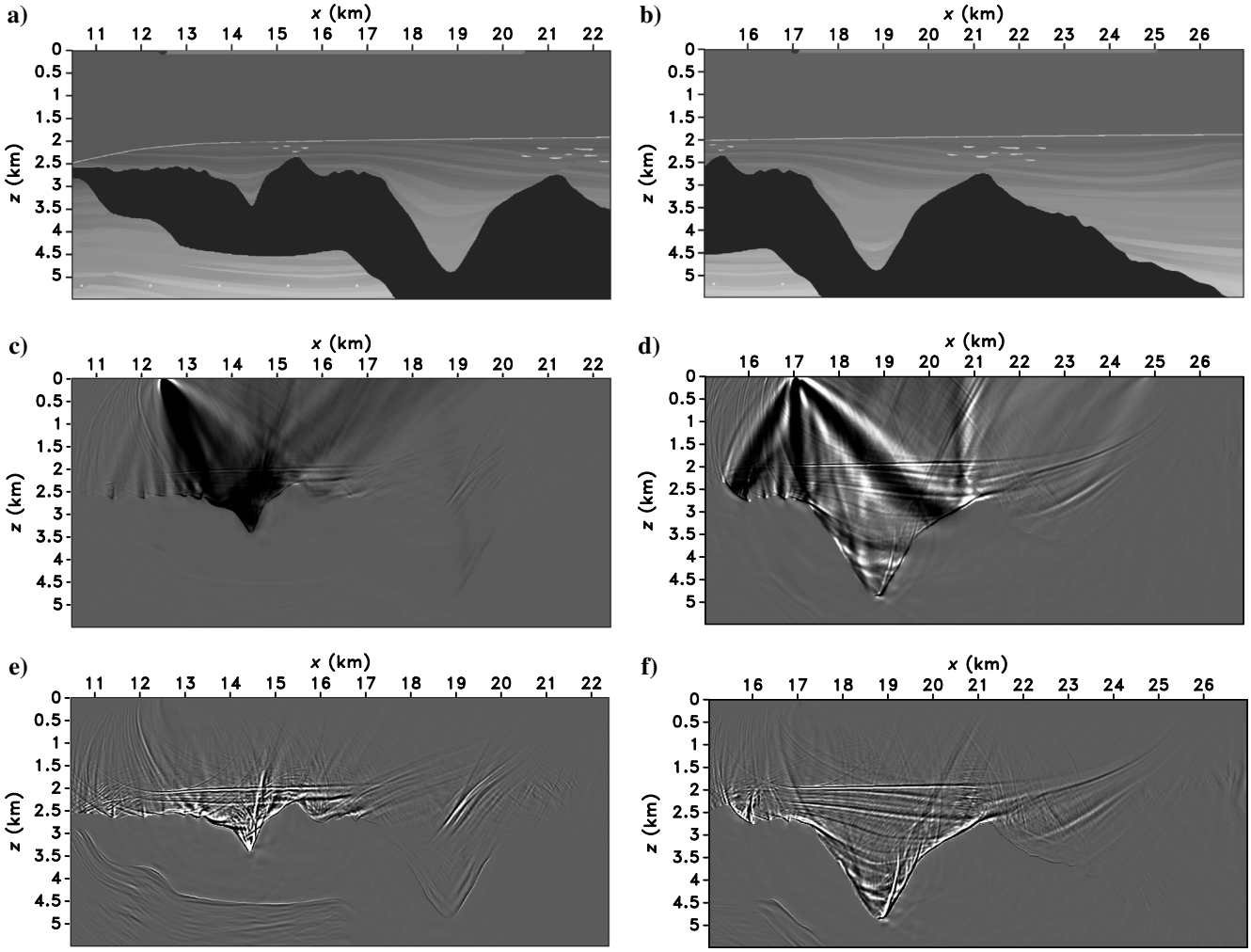


Figure 5. Single-shot Sigsbee migrations. (a and b) Sections of the stratigraphic velocity model overlaid by source and receiver positions (dark point and gray line at $x = 0$ km, respectively); (c and d) conventional images; (e and f) energy images.

Downloaded 07/18/16 to 138.67.12.184. Redistribution subject to SEG license or copyright; see Terms of Use at http://library.seg.org/

their similarity at each iteration, and then generating an optimized velocity. The difference between these two wavefields, called the data residual, is the most common form of comparison:

$$r_d = \mathbf{W}_u(u_s - u_r), \tag{37}$$

where $\mathbf{W}_u(e, \mathbf{x}, t)$ is an operator that restricts the wavefields at data locations, and $u_s(e, \mathbf{x}, t)$ and $u_r(e, \mathbf{x}, t)$ are the source and receiver wavefields, respectively. The source and receiver wavefields restricted at the receiver locations are equivalent to the synthetic and observed data, respectively. The data residual is also a function of space, time, and experiment index: $r_d(e, \mathbf{x}, t)$. These wavefields are obtained using a proper wave equation, which can be represented by the differential operator $\mathcal{L}$ that admits the adjoint operator $\mathcal{L}^{\mathrm{T}}$ for back propagation. The equations governing the wave propagation for each one of the wavefields are the physical constraints for the inverse problem (Sava, 2014):

$$\begin{bmatrix} \mathcal{F}_s \\ \mathcal{F}_r \end{bmatrix} = \begin{bmatrix} \mathcal{L} & 0 \\ 0 & \mathcal{L}^{\mathrm{T}} \end{bmatrix} \begin{bmatrix} u_s \\ u_r \end{bmatrix} - \begin{bmatrix} d_s \\ d_r \end{bmatrix} = \begin{bmatrix} 0 \\ 0 \end{bmatrix}, \tag{38}$$

where $d_s(e, \mathbf{x}, t)$ and $d_r(e, \mathbf{x}, t)$ are the forcing terms of the wave equations using $\mathcal{L}$ and $\mathcal{L}^{\mathrm{T}}$ at the source and receiver locations, respectively.

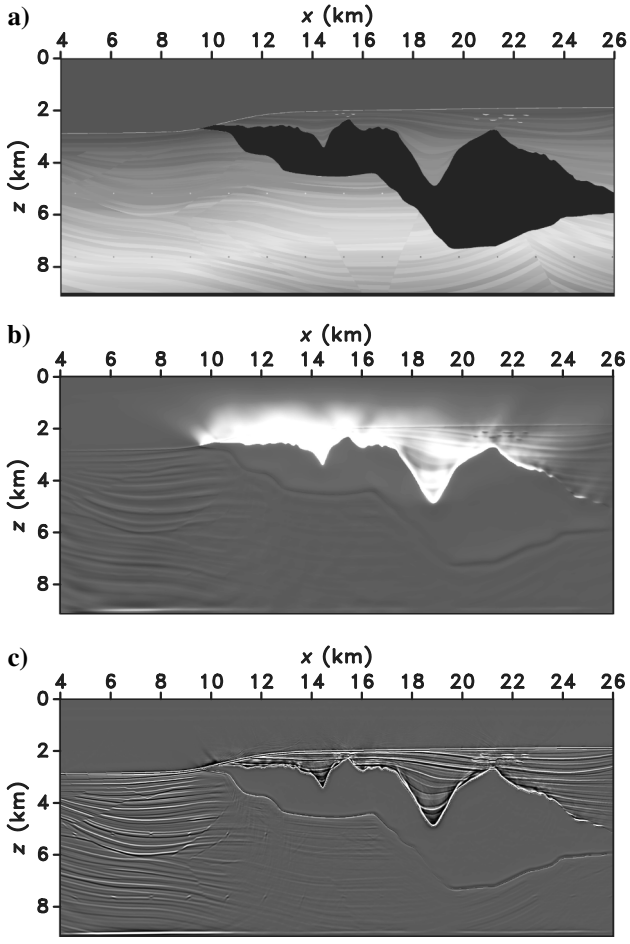


Figure 6. Multiple-shot Sigsbee migration: (a) stratigraphic velocity model, (b) conventional image, and (c) energy image.

With a residual, we can define an objective function:

$$\mathcal{J}_{L_2} = \sum_e \frac{1}{2} \|r_d\|^2_{L_2}. \tag{39}$$

To minimize the defined objective function, we need to compute its gradient with respect to model parameters. The gradient is robustly obtained by the adjoint-state method:

$$\frac{\partial \mathcal{J}}{\partial m} = -\left\langle a, \frac{\partial \mathcal{F}}{\partial m} \right\rangle, \tag{40}$$

where $m(\mathbf{x})$ is the model parameter; $\mathcal{F}$ is the physical realization equation, which can be either $\mathcal{F}_s$ or $\mathcal{F}_r$ in equation 38; $a(e, \mathbf{x}, t)$ is the adjoint-state variable; and $\langle , \rangle$ is the inner product between the adjoint-state variable and the derivative of $\mathcal{F}$ with respect to the model parameters (Plessix, 2006).

An inner product must output a scalar quantity from two vectors and must have linear properties (Jain et al., 2004). Both inner products in L_2- or L_E-norms satisfy these requirements. Therefore,

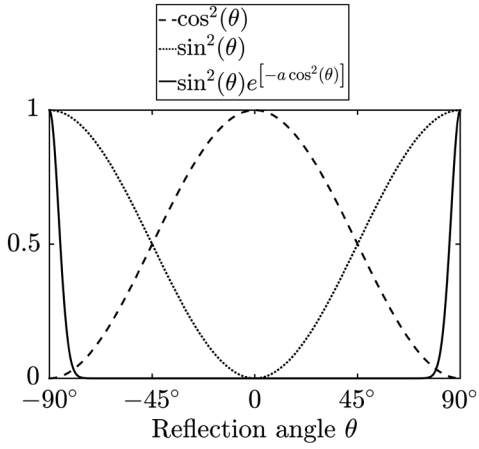


Figure 7. Plots of the angle-dependent functions of the imaging conditions in equations 33 (dotted line) and 34 (dashed line). An exponential in function of $\cos^2(\theta)$ and scaling factor $\alpha = 100$ is applied on $\sin^2(\theta)$ (solid line).

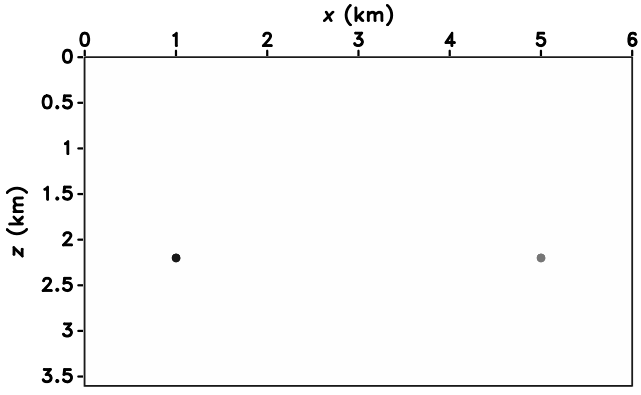


Figure 8. Geometry of the experiment in Figure 9. The black dot indicates source location and the gray dot indicates receiver location.

$$\frac{\partial \mathcal{J}}{\partial m} = -\left\langle a, \frac{\partial \mathcal{F}}{\partial m} \right\rangle_{L_2} = -\left(\frac{\partial \mathcal{F}}{\partial m}\right)^{\mathrm{T}} a \tag{41}$$

$$\frac{\partial \mathcal{J}}{\partial m} = -\left\langle a, \frac{\partial \mathcal{F}}{\partial m} \right\rangle_{E} = -\left\langle \Box a, \Box \frac{\partial \mathcal{F}}{\partial m} \right\rangle. \tag{42}$$

The adjoint-state variable $a(e, \mathbf{x}, t)$ is computed using the adjoint of the wave-equation operator in either one of the equations in equation 38. The adjoint-state variable can be defined as a_s or a_r depending on which physical constraint is used from equation 38:

$$\begin{bmatrix} \mathcal{L}^{\mathrm{T}} & 0 \\ 0 & \mathcal{L} \end{bmatrix} \begin{bmatrix} a_s \\ a_r \end{bmatrix} = \begin{bmatrix} g_s \\ g_r \end{bmatrix}, \tag{43}$$

where $g_s(e, \mathbf{x}, t)$ and $g_r(e, \mathbf{x}, t)$ are the adjoint sources, and they are defined as the derivative of the objective function with respect to state variables. We can use equation 39 to obtain the adjoint sources:

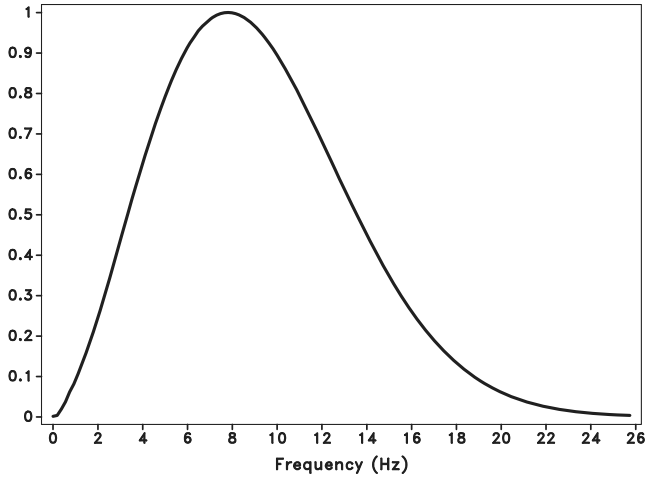


Figure 10. Normalized amplitude spectrum of the average of all traces in the observed data for the Marmousi FWI experiment. Peak frequency is approximately 9 Hz.

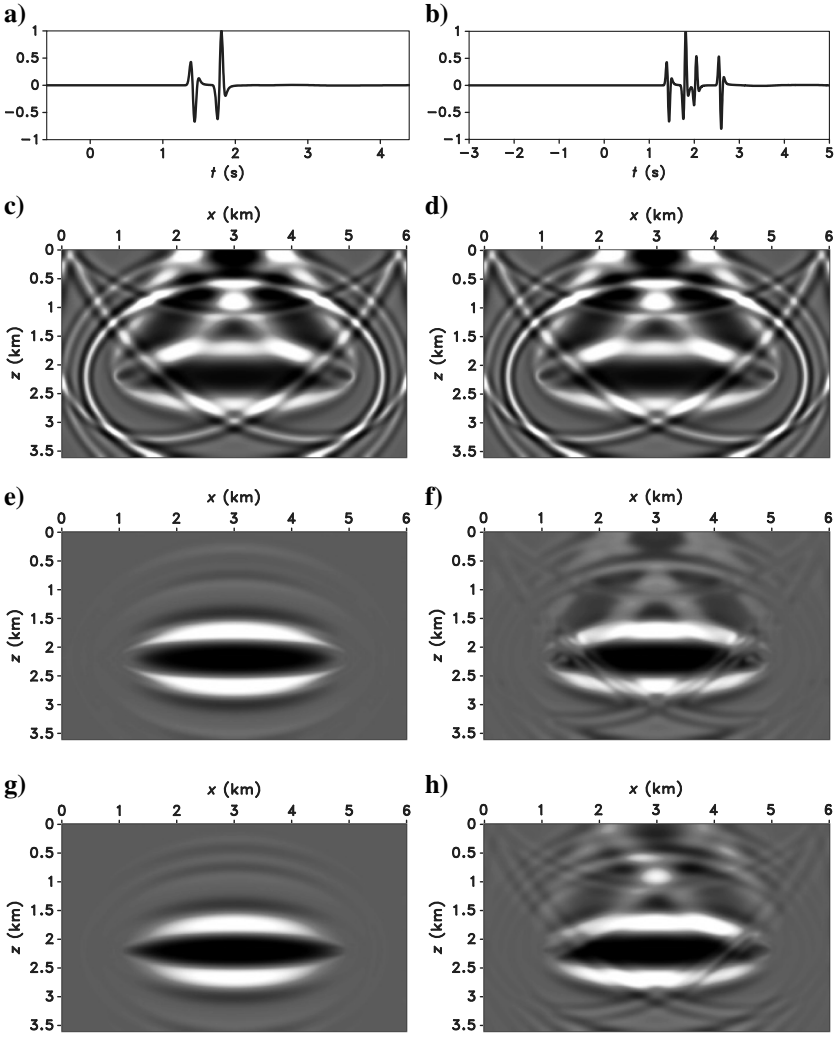


Figure 9. Simple FWI experiments with an increase of 30% in velocity from the true model, without and with a free surface at $x = 0$ km, respectively: (a and b) Data residual, (c and d) conventional FWI gradient, (e and f) energy filtered FWI gradient, with the exponential filter applied on the image, and (g and h) on the wavefields. Most of the reflection artifacts are attenuated by the filtering.

Downloaded 07/18/16 to 138.67.12.184. Redistribution subject to SEG license or copyright; see Terms of Use at http://library.seg.org/

$$\begin{bmatrix} g_s \\ g_r \end{bmatrix} = \begin{bmatrix} \frac{\partial \mathcal{J}}{\partial u_s} \\ \frac{\partial \mathcal{J}}{\partial u_r} \end{bmatrix} = \begin{bmatrix} +\mathbf{W}_u^{\mathrm{T}} \\ -\mathbf{W}_u^{\mathrm{T}} \end{bmatrix} r_d. \tag{44}$$

In summary, our goal is to compute the gradient by using equation 42 in a form that favors the tomographic term and attenuates the migration term.

Application of the energy norm imaging condition to preserve the tomographic term

In the previous section, we discuss the application of the energy norm imaging condition for attenuating a certain reflection angle, leading to a pair of complementary imaging conditions in equations 35 and 36. Because these two images are complementary with respect to angle, the maximum value of one imaging condition is the minimum value of the other imaging condition, and vice versa. We are interested in selecting a narrow range of reflection angles near 90°, i.e., from backscattering, diving, and head waves. However, the image $I_E(\mathbf{x}, \theta_c = 0^\circ)$, which has maximum amplitude at 90°, selects a broad range of reflection angles. A suitable option to make this range narrower is to apply an exponential function that has the greatest decay for angles far from 90°. The complementary image $I_E(\mathbf{x}, \theta_c = 90^\circ)$ indicates how far a certain angle is from 90°. Considering this, we can define the filtered image by an exponential function applied to $I_E(\mathbf{x}, \theta_c = 0^\circ)$ as

$$I_E^{\text{tomo}} = I_E(\mathbf{x}, \theta_c = 0^\circ) e^{-\alpha I_E(\mathbf{x}, \theta_c = 90^\circ)}, \tag{45}$$

where I_E^{tomo} stands for the tomographic component of the image. In equation 45, by inserting the complementary image $I_E(\mathbf{x}, \theta_c = 90^\circ)$ into the exponential function with a proper factor $\alpha > 1$, we are able to select a narrower range of reflection angles from $I_E(\mathbf{x}, \theta_c = 0^\circ)$, without directly computing these angles. The image inside the exponential should be normalized, such that only the $\sin^2(\theta)$ factor is accounted for in the exponential. In equations 33 and 34, the term that depends on the reflection angle for each imaging condition is $\sin^2(\theta)$ and $\cos^2(\theta)$, respectively. Figure 7 presents a plot of these terms and a plot of $\sin^2(\theta)$ with the exponential function applied. The application of the exponential function to $\sin^2(\theta)$ resembles the exponential filter application in equation 45.

The complementary relation found in equations 33 and 34 is also applicable for the source and receiver wavefields at each time step. The multipathing character of the wavefields causes different reflection angles to overlap in the image. Consequently, a more ideal procedure would involve applying exponential filtering in the wavefield domain, before stacking over time.

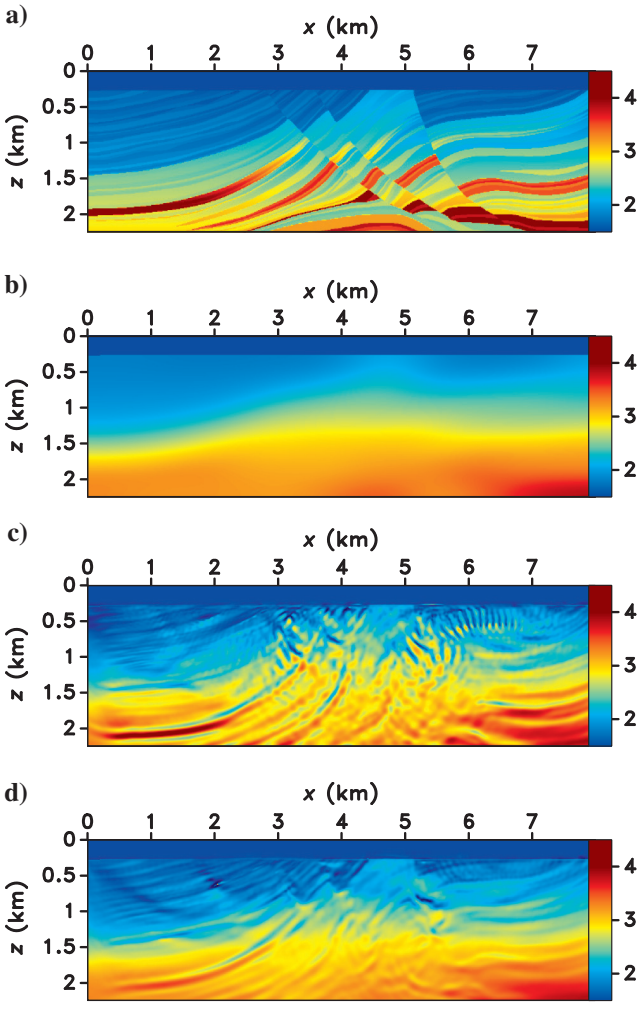


Figure 11. Velocity models used in the Marmousi FWI experiment: (a) true velocity and (b) initial velocity. Models obtained after 31 iterations: (c) conventional and (d) energy FWI.

Examples

We investigate the efficiency of the proposed FWI gradient filtering by using a very simple model with a true velocity of 2.5 km/s. Figure 8 shows experiments with a geometry consisting of one source at $x = 1$ km and one receiver at $x = 5$ km, at depth $z = 2.25$ km. The percentage of increase from the true velocity is 30% for creating the synthetic data. In Figure 9a, the data residual consists of two separated signals, one from the synthetic and the other from the observed direct wave. In Figure 9c, the wavefield constructed from the simulated data correlates with the source wavefield along the direct path between source and receiver, thus generating the well-known low-frequency waveform inversion sensitivity kernel. Similarly, the wavefield reconstructed from the observed data correlates with the source wavefield at all locations that match the total traveltime from the source to the receiver. This correlation harms the gradient by placing an apparent reflector where it does not exist; we intend to attenuate this correlation with the proposed exponential filter by selecting only the wavefield correlations at 180°. We can apply the exponential filter either in the image domain (Figure 9e) or in the wavefield domain (Figure 9g). The filter is effective in removing the reflections, though weak energy from wide-angle reflections remains. We obtain improved results with filter applied in the wavefield domain (Figure 9g). For a similar model with a free surface, we obtain the gradients in Figure 9d, 9f, and 9h. Due to multiple paths, crosstalk artifacts are visible in the conventional gradient (Figure 9d). The filtered gradients (Figure 9f and 9h) show decreased amplitude for wide-angle reflections in the image and in the wavefield domains. The factor α in the exponent function is empirically chosen for all experiments using this filtering.

Figures 10–13 show an FWI experiment for the Marmousi model (Bourgeois et al., 1991). For this synthetic experiment, we use a

Downloaded 07/18/16 to 138.67.12.184. Redistribution subject to SEG license or copyright; see Terms of Use at http://library.seg.org/

Downloaded 07/18/16 to 138.67.12.184. Redistribution subject to SEG license or copyright; see Terms of Use at http://library.seg.org/

source Ricker wavelet with peak frequency of a 9 Hz; 67 source locations at the water surface equally spaced by 120 m and the velocity model in Figure 11a to generate the observed data, which are recorded at every point at the surface. Figure 10 shows the observed data amplitude spectra. We create an initial velocity model (Figure 11b) by smoothing and applying a bulk increment of 8% on the true velocity. Figure 12 shows the FWI gradients for the first iteration, using the CIC (Figure 12a) and the energy imaging condition (Figure 12b). To avoid empirical determination of the scaling parameter α at every iteration, the energy imaging condition in equation 45 is used without the exponential factor, reducing the imaging condition to the one in equation 35. This simplification also diminishes the computational cost from the energy FWI, which becomes almost as fast as the conventional FWI. Similarly to the simple experiments in Figure 9, the energy gradient enhances the tomographic term created by diving waves and attenuates the migration term created by reflections and artifacts due to sparse shots, as one can compare in Figure 12a and 12b. At the eighth iteration, we switch the energy FWI to its conventional counterpart because the model at this iteration contains sufficient low-wavenumber features. After 31 iterations, we obtain the models in Figure 11c and 11d. The conventional FWI result (Figure 11c) contains artifacts created by the migration term, whereas the energy FWI result (Figure 11d) is a more acceptable model with attenuated artifacts. For both cases, the data objective function decreases over iterations (Figure 13). However, because the energy FWI regularizes the inversion process with a smoother model, we obtain a slightly larger data residual at the end of iterations compared to the conventional FWI.

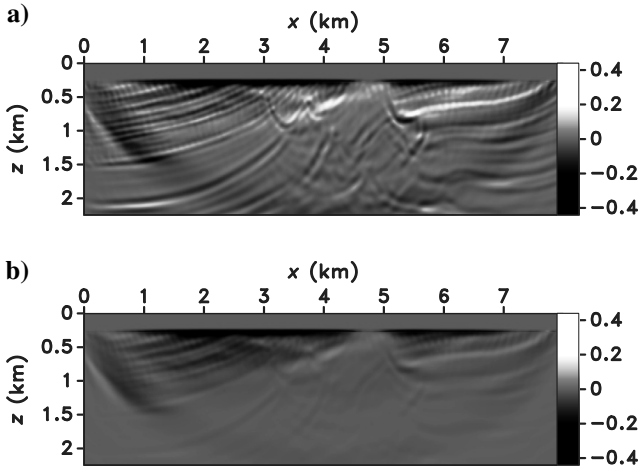


Figure 12. FWI gradients for the first iteration: (a) conventional and (b) energy FWI.

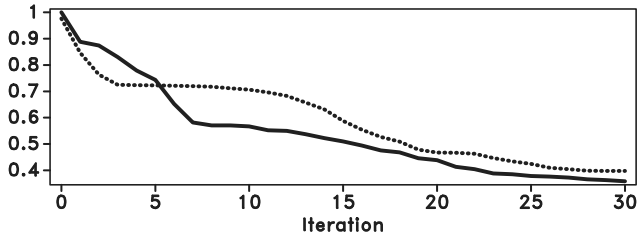


Figure 13. Normalized data objective functions over iterations for conventional (solid line) and energy (dashed line) FWI. The energy FWI switches to the conventional one at iteration 8.

CONCLUSIONS

The energy imaging condition provides an elegant and effective procedure for attenuating backscattering artifacts in RTM; this method generates an image representing the projection of 4D gradients ($\Box U$ and $\Box V$) onto one another. Our new imaging condition also offers a physical explanation for the effectiveness of the Laplacian operator in attenuating events corresponding to waves propagating along the same path. The imaging condition can also be used to attenuate an arbitrary reflection angle. Future work would involve exploiting this flexibility of the imaging condition for attenuating any reflection angle to obtain an extended image in the angle domain. The new imaging condition can also be used to generate complementary images as a function of incidence and reflection angles. This complementary property between the images enables us to filter the FWI gradient to attenuate its reflection components and favor the transmission (tomographic) component.

ACKNOWLEDGMENTS

We would like to thank sponsor companies of the Center for Wave Phenomena, whose support made this research possible. We acknowledge Antoine Guitton for helpful discussions. The reproducible numeric examples in this paper use the Madagascar open-source software package (Fomel et al., 2013) freely available from http://www.ahay.org.

APPENDIX A

RELATION WITH THE LAPLACIAN OPERATOR

One can show that the imaging condition in equation 26 is equivalent to the Laplacian filter under certain assumptions. Rewriting the imaging condition in equation 26 with continuous wavefields along time yields

$$I_E = \int_0^T [-\dot{U}\,\dot{V} + v\nabla U \cdot v\nabla V]dt, \tag{A-1}$$

where the source wavefield is oriented forward in time $U(\mathbf{x}, t)$; and the receiver wavefield is oriented backward in time $V(\mathbf{x}, T-t)$. Using integration by parts in the first term of the integrand, we have

$$\begin{aligned} -\int_0^T \dot{U}\,\dot{V}\,dt &= -[V\dot{U}q]_0^T + \int_0^T U\ddot{V}dt \\ &= -[U\dot{V}]_0^T + \int_0^T V\ddot{U}dt. \end{aligned} \tag{A-2}$$

Assuming homogeneous initial and final conditions, the wavefields and their derivatives evaluated at $t = 0$ and $t = T$ become zero. Substituting the remaining terms in equation A-1 gives

$$I_E = \int_0^T \left[\frac{1}{2} V\ddot{U} + \frac{1}{2} U\ddot{V} + v\nabla U \cdot v\nabla V\right] dt. \quad \text{(A-3)}$$

In the far-field, the source and receiver wavefields satisfy the homogeneous acoustic wave equation. Therefore,

$$I_E = \frac{1}{2}\int_0^T [v^2 V\nabla^2 U + v^2 U\nabla^2 V + 2v\nabla U \cdot v\nabla V] dt. \quad \text{(A-4)}$$

Scaling this imaging condition by $1/v^2$, we obtain

$$I_E = \frac{1}{2}\int_0^T [V\nabla^2 U + U\nabla^2 V + 2\nabla U \cdot \nabla V] dt. \quad \text{(A-5)}$$

Using calculus, we obtain

$$\nabla^2(UV) = V\nabla^2 U + U\nabla^2 V + 2\nabla U \cdot \nabla V, \quad \text{(A-6)}$$

and therefore,

$$I_E = \frac{1}{2}\nabla^2 \int_0^T UV dt = \frac{1}{2}\nabla^2 I_{L_2}, \quad \text{(A-7)}$$

which means the energy imaging condition I_E is equivalent to the Laplacian applied on the conventional image I_{L_2} by a scaling factor of $1/2$.

REFERENCES

Albertin, U., G. Shan, and J. Washbourne, 2013, Gradient orthogonalization in adjoint scattering-series inversion: 83rd Annual International Meeting, SEG, Expanded Abstracts, 1058–1062.

Alkhalifah, T., 2015, Scattering-angle based filtering of the waveform inversion gradients: Geophysical Journal International, **200**, 363–373, doi: 10.1093/gji/ggu379.

Almomin, A., and B. Biondi, 2012, Tomographic full waveform inversion: Practical and computationally feasible approach: 82nd Annual International Meeting, SEG, Expanded Abstracts, doi: 10.1190/segam2012-0976.1.

Baysal, E., D. D. Kosloff, and J. W. C. Sherwood, 1983, Reverse time migration: Geophysics, **48**, 1514–1524, doi: 10.1190/1.1441434.

Bourgeois, A., M. Bourget, P. Lailly, M. Poulet, P. Ricarte, and R. Versteeg, 1991, Marmousi, model and data: Presented at the 1990 EAGE Workshop on Practical Aspects of Seismic Data Inversion.

Brandsberg-Dahl, S., N. Chemingui, D. Whitmore, S. Crawley, E. Klochikhina, and A. Valenciano, 2013, 3D RTM angle gathers using an inverse scattering imaging condition: 83rd Annual International Meeting, SEG, Expanded Abstracts, 3958–3962.

Chang, W.-F., and G. A. McMechan, 1986, Reverse-time migration of offset vertical seismic profiling data using the excitation-time imaging condition: Geophysics, **51**, 67–84, doi: 10.1190/1.1442041.

Chappel, J., A. Iqbal, and D. Abbot, 2010, A simplified approach to electromagnetism using geometric algebra, http://arxiv.org/abs/1010.4947v2, accessed 12 February 2015.

Clærbout, J. F., 1985, Imaging the earth's interior: Blackwell Scientific Publications.

Cohen, J. K., and N. Bleistein, 1979, Velocity inversion procedure for acoustic waves: Geophysics, **44**, 1077–1087, doi: 10.1190/1.1440996.

Costa, J. C., F. A. S. Neto, M. Alcantara, J. Schleicher, and A. Novais, 2009, Obliquity-correction imaging condition for reverse time migration: Geophysics, **74**, no. 3, S57–S66, doi: 10.1190/1.3110589.

Diaz, E., and P. Sava, 2015, Wavefield tomography using reverse time migration backscattering: Geophysics, **80**, no. 1, R57–R69, doi: 10.1190/geo2014-0100.1.

Douma, H., D. Yingst, I. Vasconcelos, and J. Tromp, 2010, On the connection between artifact filtering in reverse-time migration and adjoint tomography: Geophysics, **75**, no. 6, S219–S223, doi: 10.1190/1.3505124.

Evans, L. C., 1997, Partial differential equations: American Mathematical Society.

Feynman, R. P., R. B. Leighton, and M. Sands, 1964, The Feynman lectures on physics: Addison Wesley.

Fletcher, R. F., P. Fowler, P. Kitchenside, and U. Albertin, 2005, Suppressing artifacts in prestack reverse time migration: 75th Annual International Meeting, SEG, Expanded Abstracts, 2049–2051.

Fomel, S., P. Sava, I. Vlad, Y. Liu, and V. Bashkardin, 2013, Madagascar: Open-source software project for multidimensional data analysis and reproducible computational experiments: Journal of Open Research Software, **1**, e8, doi: 10.5334/jors.ag.

Gao, F., P. Williamson, and H. Houllevigue, 2012, Full waveform inversion by deconvolution gradient method: 82nd Annual International Meeting, SEG, Expanded Abstracts, doi: 10.1190/segam2012-1408.1.

Gauthier, O., J. Virieux, and A. Tarantola, 1986, Two-dimensional nonlinear inversion of seismic waveforms: Numerical results: Geophysics, **51**, 1387–1403, doi: 10.1190/1.1442188.

Guitton, A., B. Kaelin, and B. Biondi, 2007, Least-squares attenuation of reverse-time-migration artifacts: Geophysics, **72**, no. 1, S19–S23, doi: 10.1190/1.2399367.

Hindlet, F., and P. Kolb, 1988, Inversion of prestack field data: An application to 1-D acoustic media: 58th Annual International Meeting, SEG, Expanded Abstracts, 1073–1076.

Jain, P. K., O. P. Ahuja, and K. Ahmed, 2004, Functional analysis (2nd ed.): New Age International.

Lailly, P., 1983, The seismic inverse problem as a sequence of before stack migrations: Conference on inverse scattering, theory and application: Presented at SIAM, Expanded Abstracts, 206–220.

Levin, S. A., 1984, Principle of reverse-time migration: Geophysics, **49**, 581–583, doi: 10.1190/1.1441693.

Liu, F., G. Zhang, S. A. Morton, and J. P. Leveille, 2011, An effective imaging condition for reverse-time migration using wavefield decomposition: Geophysics, **76**, no. 1, S29–S39, doi: 10.1190/1.3533914.

Margrave, G. F., and R. J. Ferguson, 1999, Wavefield extrapolation by nonstationary phase shift: Geophysics, **64**, 1067–1078, doi: 10.1190/1.1444614.

McMechan, G. A., 1983, Migration by extrapolation of time-dependent boundary values: Geophysical Prospecting, **31**, 413–420, doi: 10.1111/j.1365-2478.1983.tb01060.x.

McOwen, R. C., 2003, Partial differential equations: Methods and applications (2nd ed.): Prentice Hall.

Mora, P., 1989, Inversion = migration + tomography: Geophysics, **54**, 1575–1586, doi: 10.1190/1.1442625.

Oristaglio, M. L., 1989, An inverse scattering formula that uses all the data: Inverse Problems, **5**, 1097–1105, doi: 10.1088/0266-5611/5/6/015.

Perrone, F., and P. Sava, 2015, Wavefield tomography based on local image correlations: Geophysical Prospecting, **63**, 35–54, doi: 10.1111/1365-2478.12163.

Pestana, R., A. W. G. dos Santos, and E. S. Araujo, 2013, RTM imaging condition using impedance sensitivity kernel combined with Poynting vector: Presented at 13th International Congress of the Brazilian Geophysical Society.

Plessix, R. E., 2006, A review of the adjoint-state method for computing the gradient of a functional with geophysical applications: Geophysical Journal International, **167**, 495–503, doi: 10.1111/j.1365-246X.2006.02978.x.

Plessix, R. E., Y.-H. de Roech, and G. Chavent, 1998, Waveform inversion of reflection seismic data for kinematic parameters by local optimization: SIAM Journal on Scientific Computing, **20**, 1033–1052, doi: 10.1137/S1064827596311980.

Plessix, R. E., P. Milcik, H. Rynja, A. Stopin, K. Matson, and S. Abri, 2013, Multiparameter full-waveform inversion: Marine and land examples: The Leading Edge, **32**, 1030–1038, doi: 10.1190/tle32091030.1.

Sava, P., 2014, A comparative review of wavefield tomography methods: Center for Wave Phenomena.

Sava, P., and S. Fomel, 2006, Time-shift imaging condition in seismic migration: Geophysics, **71**, no. 6, S209–S217, doi: 10.1190/1.2338824.

Sava, P., and I. Vasconcelos, 2011, Extended imaging conditions for wave-equation migration: Geophysical Prospecting, **59**, 35–55, doi: 10.1111/j.1365-2478.2010.00888.x.

Suh, S. Y., and J. Cai, 2009, Reverse-time migration by fan filtering plus wavefield decomposition: 79th Annual International Meeting, SEG, Expanded Abstracts, 2804–2808.

Sun, S., and B. Wang, 2013, Improving salt boundary imaging using an RTM inverse scattering imaging condition: 83rd Annual International Meeting, SEG, Expanded Abstracts, 3953–3957.

Downloaded 07/18/16 to 138.67.12.184. Redistribution subject to SEG license or copyright; see Terms of Use at http://library.seg.org/

Tang, Y., S. Lee, A. Baumstein, and D. Hinkley, 2013, Tomographically enhanced full wavefield inversion: 83rd Annual International Meeting, SEG, Expanded Abstracts, 1037–1041.
Tanushev, N. M., B. Engquist, and R. Tsai, 2009, Gaussian beam decomposition of high frequency wave fields: Journal of Computational Physics, **228**, 8856–8871, doi: 10.1016/j.jcp.2009.08.028.
Tarantola, A., 1984, Inversion of seismic reflection data in the acoustic approximation: Geophysics, **49**, 1259–1266, doi: 10.1190/1.1441754.
Vyas, M., X. Du, E. Mobley, and R. Fletcher, 2011, Methods for computing angle gathers using RTM: Presented at the 73rd Annual International Conference and Exhibition, EAGE.
Whitmore, N. D., and S. Crawley, 2012, Applications of RTM inverse scattering imaging conditions: 82nd Annual International Meeting, SEG, Expanded Abstracts, doi: 10.1190/segam2012-0779.1.
Xu, S., F. Chen, B. Tang, and G. Lambare, 2014, Noise removal by migration of time-shift images: Geophysics, **79**, no. 3, S105–S111, doi: 10.1190/geo2012-0497.1.
Yang, T., and P. Sava, 2015, Image-domain wavefield tomography with extended common-image-point gathers: Geophysical Prospecting.
Yoon, K., and K. J. Marfurt, 2006, Reverse-time migration using the Poynting vector: Exploration Geophysics, **37**, 102–107, doi: 10.1071/EG06102.
Youn, O., and H. W. Zhou, 2001, Depth imaging with multiples: Geophysics, **66**, 246–255, doi: 10.1190/1.1444901.
Zeidler, E., 1999, Applied functional analysis: Applications to mathematical physics: Springer.
Zhang, Q., 2014, RTM angle gathers and specular filter (SF) RTM using optical flow: 84th Annual International Meeting, SEG, Expanded Abstracts, 3816–3820.
Zhang, Y., and J. Sun, 2009, Practical issues in reverse time migration: True amplitude gathers, noise removal and harmonic source encoding: First Break, **27**, 53–59, doi: 10.3997/1365-2397.2009002.

Downloaded 07/18/16 to 138.67.12.184. Redistribution subject to SEG license or copyright; see Terms of Use at http://library.seg.org/